Available online at www.sciencedirect.com
SCIENCE DIRECT®
International Journal of Heat and Mass Transfer 47 (2004) 2457–2467
International Journal of HEAT and MASS TRANSFER
www.elsevier.com/locate/ijhmt

Measurement of solute diffusivities. Part III. From solutal convection dominated transport to quasi-diffusive transport

V. Botton *, P. Lehmann, R. Bolcato, R. Moreau

EPM-Madylam, ENSHMG, BP 95, 38402 Saint Martin d'Heres Cedex, France

Received 14 June 2002

Abstract

This paper presents an analytical and experimental investigation of the new ground-based method for diffusion measurements in liquid metals presented in the two companion papers [Int. J. Heat Mass Transfer 17 (2001) 1639] and [Int. J. Heat Mass Transfer 44 (2001) 3345]. The configuration under consideration is a horizontal capillary tube submitted to a vertical steady magnetic field; the temperature field is assumed isothermal. The aim of this third part is to introduce a single description of transport in a diffusion experiment over a wide range of parameters (namely magnetic field intensity and experimental duration), which overlaps both the two asymptotic models previously presented. The experimental results, obtained in two different apparatus, are in good agreement with the analytical model and exhibit a fair repeatability. The impurity diffusion coefficient of Bi in Sn is measured at 275 °C and near the fusion point, in good agreement with recent microgravity data.

1. Introduction: summary and limits of previous studies

Despite the importance of molecular diffusivity data for fluid physics and solidification modelling, measurements reported in the literature show a large scatter [1]. These experiments basically consist in mixing a pure metal and one of its alloys in purely diffusive conditions. In practice, however, diffusive transport is usually so slow that even very weak convection can have a significant effect on the experimental results. Liquid metals and semiconductors are particularly sensitive to thermal convection, due to the high operating temperature in the experiments. As diffusion experiments necessarily involve a concentration gradient, one is likely to observe transport also by solutal convection. Until now, the best way to limit the effects of natural convection has been to perform the experiments in microgravity. For good electrical conductors, however, the use of a steady magnetic field to brake the convective motion offers an attractive ground-based alternative.

The basis of the proposed method has been presented in two companion papers [2,3]. The main principle is to carefully control and quantify the convective transport in the experiment, rather than to completely suppress it. To achieve this, a model has been derived to predict the apparent diffusivity measured in a diffusion experiment in the presence of convection. The experiment requires accurate control of the convection to impose a well-defined flow, which can be used as input to the analytical model.

The considered geometry is a horizontal capillary tube (2 mm in diameter, 200 mm in length) located in a shear cell [6]. When the experiment starts, half of the capillary tube is filled with pure liquid metal, and it is brought into contact with the other half of the tube, which contains a homogeneous binary alloy. The initial concentration profile along the tube is thus a step of height Δc_0 The very strong horizontal density gradient generates a buoyancy-driven motion. This motion always enhances the mixing, relative to purely diffusive

* Corresponding author. Address: LMFA, INSA de Lyon, bât. J. Jacquard, 20 av. A. Einstein, 69621 Villeurbanne, France. Tel.: +33-4-72-43-70-19; fax: +33-4-72-43-87-52.
E-mail address: valery.botton@insa-lyon.fr (V. Botton).

0017-9310/$ - see front matter © 2003 Elsevier Ltd. All rights reserved.
doi:10.1016/j.ijheatmasstransfer.2003.10.037

Nomenclature

B	magnetic field intensity
c_0	cross-section averaged concentration expressed in weight fraction
C_0	reduced cross-section averaged concentration
C_{max}	maximum concentration, the minimum concentration being zero
D	true molecular diffusivity
D_{app}	apparent diffusivity
f_0	slope of f at its origin
G	characteristic concentration gradient
Gr_S	solutal Grashof number
H	capillary tube diameter
Ha	Hartmann number
I	integral of f on the half space
L	half length of the capillary tube
S	modified solutal Rayleigh number
Sc	Schmidt number
t	time elapsed after the contact of the two elements
$t^* = \tau/S^2$	re-scaled time for comparison with [2]
W	characteristic longitudinal velocity
X	axial coordinate along the cylinder
x	non-dimensional axial coordinate along the cylinder
$x^* = X/S$	axial coordinate re-scaled for comparison with [2]
x_0	possible shift of the experimental profile with respect to zero
α	correction factor for moderate Ha number
β	solutal expansion coefficient
$\delta^* = \delta/S$	mixing length, re-scaled for comparison with [2]
Δc_0	initial step in solutal concentration
$\eta = X/\delta$	similarity variable
ν	kinematic viscosity
ρ	density
σ	electrical conductivity
τ	non-dimensional time elapsed after the contact of the two elements

transport. The concentration gradient in the liquid decreases with time and the convective transport diminishes. Asymptotically, as time goes to infinity, transport tends towards pure diffusion, and the composition tends towards homogeneity. After a specified duration, t, the experiment is terminated by separating the liquid column into small segments. Each segment then solidifies independently from its neighbours. The average chemical composition of the solidified segments is analysed to obtain a concentration profile $c_0(x,t)$ along the capillary tube. The apparent diffusivity, D_{app}, is deduced by fitting this profile to an error function, the latter being the analytic solution to the 1D diffusion equation in an infinite medium with an initial step in concentration.

Due to additional transport by convection, the apparent diffusivity D_{app} is always greater than the true diffusivity, D. The stronger the convection during the experiment, the larger the difference between D_{app} and D; as shown by Barat and Garandet [4]; this difference scales as:

$$D_{app} - D \sim kH^2W^2/D^2, \tag{1}$$

where W is a characteristic convection velocity.

The proposed method uses a vertical steady magnetic field, of intensity B, to damp the flow. For a characteristic concentration gradient G, W varies as GB^{-2}. With G estimated as $\Delta c_0/(D_{app}t)^{1/2}$, the velocity W scales as:

$$W \sim GB^{-2} = \Delta c_0/(D_{app}t)^{1/2}B^{-2}. \tag{2}$$

Since W depends on t, it follows from relation (1) that D_{app} is also time dependent; the measured coefficient is thus a function of the duration of the experiment.

In the limit of strong convective mixing, (1) reduces to $D_{app} \sim kH^2W^2/D^2$, since $D_{app} \gg D$. The use of (2) then allows the derivation of an order-of-magnitude estimate of the apparent diffusivity:

$$D_{app} \sim \Delta c_0 t^{-1/2}B^{-2}. \tag{3}$$

An analytical solution for this asymptotic case is presented in Part I [2]. The experimental results for diffusion of Bi in Sn presented in Part II [3] confirms the B^{-2} dependence in (3), although the time dependence of the apparent diffusivity suggests an exponent -0.4, rather than the expected $-1/2$. This discrepancy is attributed to non-zero molecular diffusion in the axial direction (which is to be verified in the present paper).

In the limit of a vanishing convective contribution (large t or B), on the other hand, the apparent diffusion coefficient tends towards the true diffusion coefficient, D. As illustrated in Fig. 1, this behaviour would result in a change of the slope in a plot of $D_{app} = f(B^{-2})$. The true diffusivity is reached for an infinite magnetic field intensity, corresponding to the origin of the curve, where the tangent is expected to be horizontal.

The two asymptotic regimes described above were numerically observed in Part I [2]. No single analytical

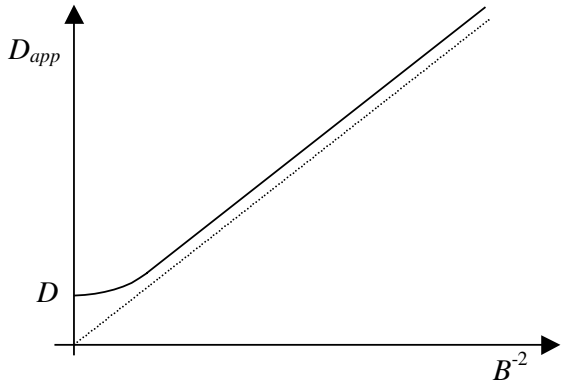

Fig. 1. Expected behaviour of the apparent diffusion coefficient as a function of the magnetic field intensity.

solution could be found describing both the quasi-diffusive, and the strongly convective regimes. In the experiments reported in Part II [3], the magnetic damping is not strong enough to observe any significant departure from the B^{-2} law; stronger fields have to be reached to demonstrate the expected change in slope.

The purpose of this paper is twofold. Firstly, we present an analytical solution joining the two asymptotic regimes. Secondly, we describe a new apparatus dedicated to diffusion experiments in higher magnetic fields and present results obtained with this new apparatus. The results obtained with our two different experimental set-ups are in close agreement. This illustrates how the proposed method can improve reproducibility, and reduce statistical scatter in molecular diffusivity data.

2. An analytical model joining the two asymptotic solutions

2.1. Hypothesis and notations

This section is devoted to the prediction of the axial concentration profile after a given time after the contact between the two fluids; it is thus concerned with transport of the cross-section averaged concentration C_0. The hypotheses and notations are the same as in [3], although no temperature gradient is considered here. The definitions of non-dimensional parameters are also retained. In particular, the Grashof number is expressed as $Gr_S = g\beta\Delta c_0/LH^4/\nu^2$. The typical core velocity at time τ and location X along the capillary scales as $Gr_S/Ha^2\partial C_0/\partial X$, where the Hartmann number $Ha = [\sigma/(\rho\nu)]^{1/2}BH$ accounts for the electromagnetic damping. The influence of the velocity field on the longitudinal transport is characterised by the parameter $S = \alpha^{1/2}Gr_S Sc/Ha^2$, featuring the Schmidt number Sc and a coefficient $\alpha(Ha)$. The latter accounts for the geometry and the shape of the velocity profile in the cross-section [2].

2.2. Solution of the transport equation

Let us start with the transport equation derived in Part II (Eq. (13) of Ref. [3], with $T = 0$ since we assume isothermal conditions):

$$\frac{\partial C_0}{\partial \tau} = \frac{\partial}{\partial X}\left\{\left[1 + \left(S\frac{\partial C_0}{\partial X}\right)^2\right]\frac{\partial C_0}{\partial X}\right\}. \tag{4}$$

This is a diffusion equation featuring an effective diffusivity $[1 + (S\partial C_0/\partial X)^2]$, which varies in time and space. As this diffusivity depends on the location along the capillary tube, the concentration profile is not an error function. Even for strong solutal convection, however, the true profile shape is very similar to an error function. This is illustrated in Fig. 2, where an error function profile is plotted together with the analytical solution of (4) assuming $(S\partial C_0/\partial X)^2 \gg 1$ [2]. From an experimental standpoint, the difference between the real profile and an erf fit is observed to be comparable with the typical uncertainty in the concentration measurements, achieved for example by *inductively coupled plasma* (ICP) analysis. In the following, the experimental concentration profiles have been analysed using a least-mean-squares fit to an error function.

The necessity of choosing some function f to approximate the solution of Eq. (4) leads us to seek a self-similar solution to the equation. We thus assume that the solution may be written as:

$$C_0 = f(\eta) \quad \text{with } \eta = X/\Delta(\tau). \tag{5}$$

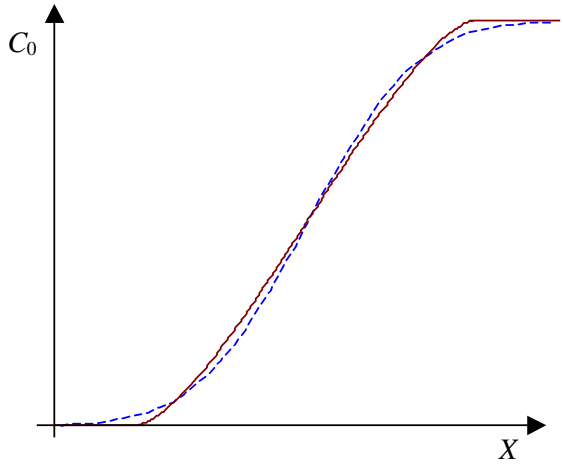

Fig. 2. Comparison of the theoretical concentration profile in an infinite medium in the case of pure diffusion (dashed line, Eq. (14)) or dominant solutal convection (full line, Eq. (15)).

For a given function f, the remaining unknown of the problem is the time dependence of Δ. The function f must feature the main properties of the experimental concentration profiles: it is a monotonic odd function and it tends towards $\pm 1/2$ as η tends towards $\pm\infty$, where its derivatives vanish.

Let us choose a large enough abscissa X_0 in the vicinity of which the variations of $C_0(X,\tau)$ are negligible. Integration of Eq. (4) between 0 and X_0 yields:

$$\int_0^{X0} \frac{\partial C_0}{\partial \tau}\,\mathrm{d}X = \left\{ \left[1 + \left(S \frac{\partial C_0}{\partial X} \right)^2 \right] \frac{\partial C_0}{\partial X} \right\}_0^{X_0}. \tag{6}$$

Introducing the slope at the origin, f_0', the right-hand side of (6) can be re-written as:

$$-f_0'/\Delta[1 + (Sf_0'/\Delta^2)^2]. \tag{7}$$

The derivation and integration operators can be permuted in the left-hand side of (6), and we can make the change of variable:

$$\begin{aligned} \int_0^{X0} \frac{\partial C_0}{\partial \tau}\,\mathrm{d}X &= \frac{\partial}{\partial \tau}\left(\Delta \int_0^{X_0/\Delta} f\,\mathrm{d}\eta \right) \\ &= \frac{\partial}{\partial \tau}\left(\Delta \frac{X_0}{2} - \int_0^{X_0/\Delta} \left(\frac{1}{2} - f(\eta) \right) \mathrm{d}\eta \right). \end{aligned} \tag{8}$$

The quantity $I = \int_0^{+\infty} (\frac{1}{2} - f(\eta))\,\mathrm{d}\eta$ is a characteristic of the chosen function f. We note that this should be a definite integral, which adds yet another desired property of f to those already listed above. Passing to the limit of infinite X_0, (6) becomes eventually:

$$\Delta\Delta' = f_0'/I[1 + (Sf_0'/\Delta^2)^2]. \tag{9}$$

Solution of (9) with the initial condition $\Delta(0) = 0$ yields:

$$\frac{I}{f_0'}\Delta^2 - f_0' S^2 I \ln\left(1 + \frac{\Delta^2}{f_0'^2 S^2} \right) = 2\tau. \tag{10}$$

2.3. Comparison with the numerical simulation by Maclean and Alboussière [2]

The definition of the similarity variable $\eta = X/\Delta(\tau)$ in (5) bonds the parameter Δ to the physical extension of the composition variations. The chosen function f provides the link between $\Delta(\tau)$ and the slope of the concentration profile at the origin. A full analysis of the problem can then be achieved in terms of this non-dimensional length, $\Delta(\tau)$. This corresponds to the analysis presented in [2], after the rescaling $x^* = X/S$ and $t^* = \tau/S^2$ which aims at giving Eq. (6) a universal form:

$$\frac{\partial C_0}{\partial t^*} = \frac{\partial}{\partial X^*}\left\{ \left[1 + \left(\frac{\partial C_0}{\partial X^*} \right)^2 \right] \frac{\partial C_0}{\partial X^*} \right\}. \tag{11}$$

Denoting $\delta^* = \Delta/S$, the solution (10) becomes

$$\frac{I}{f_0'}\delta^{*2} - f_0' I \ln\left(1 + \frac{\delta^{*2}}{f_0'^2} \right) = 2\tau. \tag{12}$$

A realistic shape can be given to f using either one of the two asymptotic solutions of the transport equation, namely:

Case a: The profile with vanishing solutal convection (i.e. driven by pure diffusion) is of the form:

$$f(\eta) = 1/2\,\mathrm{erf}(\eta/2), \tag{13}$$

then, $I = \pi^{-1/2}$ and $f_0' = (4\pi)^{-1/2}$.

Case b: The profile with strong solutal convection (i.e. negligible longitudinal diffusion) is of the form:

$$f(\eta) = 1/2 + \eta/2\sqrt{\frac{1}{\pi} - \frac{\eta^2}{4}} + \frac{1}{\pi}\arcsin\left(\frac{\sqrt{\pi}}{2}\eta \right) \quad \text{for } \eta \in \left[-\frac{2}{\sqrt{\pi}}, \frac{2}{\sqrt{\pi}} \right], \tag{14}$$

then, $I = 4/3\pi^{3/2}$ and $f_0' = \pi^{-1/2}$.

The approximate solution (12) is plotted in Fig. 3 together with the numerical solution of (11). The curve relevant to *case a* is plotted as a dashed line, the one relevant to *case b* as a dashed–dotted line, and the numerical result by Maclean and Alboussière [2] is plotted as a full line. *Case a* and the numerical solution can hardly be distinguished. Indeed, for a given value of δ^*, the relative difference between the two corresponding values of τ is less than 5% for $10^{-2} < t^* < 10^3$ and varies from 5% to 11% between $t^* = 10^{-2}$ and $t^* = 10^{-3}$. A slightly larger difference is observed between *case b* and the two others. The difference vanishes for small values

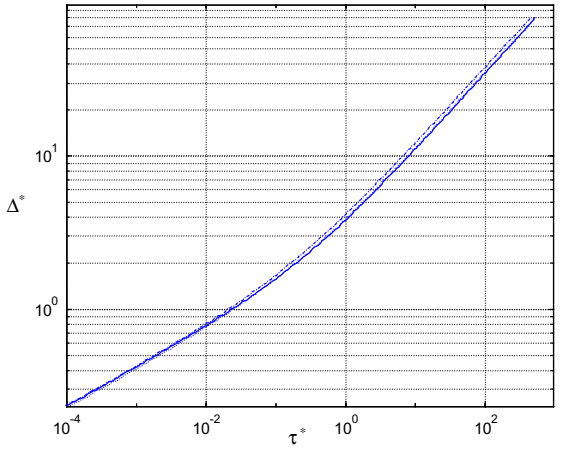

Fig. 3. Comparison between the numerical solution of Eq. (11) from [2] (full line) and the present analytical model with an erf (dashed line, Eq. (13)) or the Maclean and Alboussière function (dash–dotted line, Eq. (14)).

of t^* (say $t^* < 10^{-2}$), as can be expected from a physical standpoint since the effect of solutal convection get stronger for small t^*.

The asymptote for strong solutal convection can be recovered by expanding the logarithm in (12) for small values of δ^*, which leads to the expression

$$\delta^* = \left[4f_0'^3/It^*\right]^{1/4} \quad \text{or equivalently} \quad \Delta = (4f_0'^3/I)^{1/4}\tau^{1/4}S^{-1/2}. \tag{15}$$

The asymptote for weak solutal convection is found by neglecting the logarithm compared to the δ^{*2} term (provided that I and f_0' are both of the order of 1), which yields:

$$\delta^* = \left[2f_0'/It^*\right]^{1/2} \quad \text{or equivalently} \quad \Delta = \tau^{1/2}. \tag{16}$$

2.4. Link with the apparent diffusion coefficient

The experimental procedure is based on a fit of an error function to the experimental concentration profile, which allows the calculation of an apparent diffusion coefficient [3]. The set of apparent diffusion coefficients $D_{\text{app}}(B,t)$ obtained from a succession of experiments can then be analysed by comparison with the present model, in *case a*. The choice of *case a* relies on the fact that this introduces no further approximation than the erf-fitting procedure. The link between the measured apparent diffusion coefficient and the mixing-length $\Delta(\tau)$ is found by analogy between the erf solution of the diffusion equation and the model profile (13):

$$D_{\text{app}}/D = \Delta^2/\tau. \tag{17}$$

We can now express relation (10) in terms of the apparent diffusion coefficient:

$$\frac{D_{\text{app}}}{D} = 1 + \frac{S^2}{4\pi\tau}\ln\left(1 + \frac{4\pi\tau}{S^2}\frac{D_{\text{app}}}{D}\right). \tag{18}$$

The asymptotic expressions (15) and (16) become, respectively, $\frac{D_{\text{app}}}{D} = \frac{S\tau^{-1/2}}{\sqrt{2\pi}}$ for strong solutal convection (i.e. negligible longitudinal diffusion), $\frac{D_{\text{app}}}{D} = 1$ for vanishing solutal convection (i.e. pure diffusion).

The single equation (18) describes the evolution of the concentration profile from the solutal convection dominated regime to the molecular diffusion dominated regime. Moreover, it does not introduce any approximation other than those already made through the experimental process.

2.5. Experimental process

Eq. (18) expresses D_{app} as a function of $S/(4\pi\tau)^{1/2}$. This group is proportional to $\alpha^{0.5}B^{-2}$. This yields the idea of the diffusivity measurement method. Several experiments performed with different magnetic field intensities give an experimental $D_{\text{app}} = f(\alpha^{0.5}B^{-2})$ curve. The shape of this curve is similar to that of Fig. 1. A least-mean-squares fit of the model to this curve provides the true diffusivity D (which is the value at the origin of the curve). Fig. 1 suggests that an accurate determination of D requires some data in the very left part of the curve, in order to capture the curvature caused by an increased influence of molecular diffusion. This can be achieved using either very high magnetic field intensities, or long durations of the mixing experiments. According to [3], the duration and the magnetic flux density should fulfil the condition

$$\tau \gg S^2 = \alpha Gr^2 Sc^2/Ha^4. \tag{19}$$

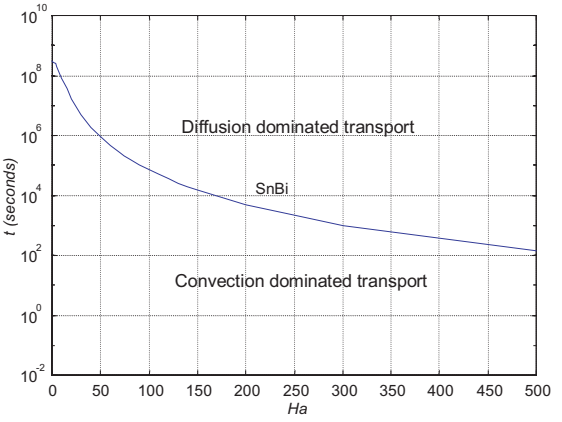

Fig. 4. Limit between the two asymptotic behaviours in the case of impurity diffusion of Bi (1 wt.%) in Sn from Eq. (19).

The limit given by (19) is plotted in Fig. 4 for the case of impurity diffusion of Bi (1 wt.%) in Sn, which is used here as a test diffusion couple. For a realistic experiment duration, like 10^5 s (~30 h), it can be seen from this plot that Hartmann numbers of the order of 150 are needed for (19) to be true. In the case of a 2 mm diameter capillary, the corresponding magnetic field intensity is around 2 T. Let us recall that the maximum field strength obtained in our earlier experimental set up [3] was 0.75 T, giving $Ha = 55$; this explains why the curvature of the $D_{\text{app}}(B,t)$ law could not be observed.

3. A new set-up featuring higher uniform magnetic fields

A new experiment, Euridice II, has been designed, including both an electromagnet and a new "shear-cell + furnace" system. The integrated design of the magnet and the furnace resulted in a particularly compact apparatus in which the production of the magnetic field is efficient without compromising the accuracy of the temperature control.

3.1. The magnet

The most powerful DC current generator available in the EPM-MADYLAM laboratory is a 80 kW (20 V, 4000 A) power supply. We adapted the electromagnet to these characteristics, the goal being to create a field of more than 2 T, uniform along the length of the capillary tube. The size of the magnetised volume is $(70\times70\times400)$ mm^3. The technique used to make the electromagnet coils is inspired by the so-called Bitter technique, usually involved in the design of solenoids. A number (136) of 2 mm thick C-shaped copper plates are used to make rectangular coils (see Fig. 5). The plates are tin-welded together, one after the other, at their 12 cm ends to form a 140 mm thick "rectangular solenoid". A 100 μm thick plastic film is put between the plate layers to achieve electrical insulation. The solenoid is cooled by water flowing through 140 holes, of diameter 2 mm, drilled in each of the copper plates. The alignment of the holes is chosen to allow circulation through the pile of plates (no particular insulation is necessary, since the conductivity of water is much lower than that of copper). The solenoid is contained in a tight stainless steel box through which the cooling water is forced. This particular magnet design is far more compact than a conventional design, using copper wires and water tubes.

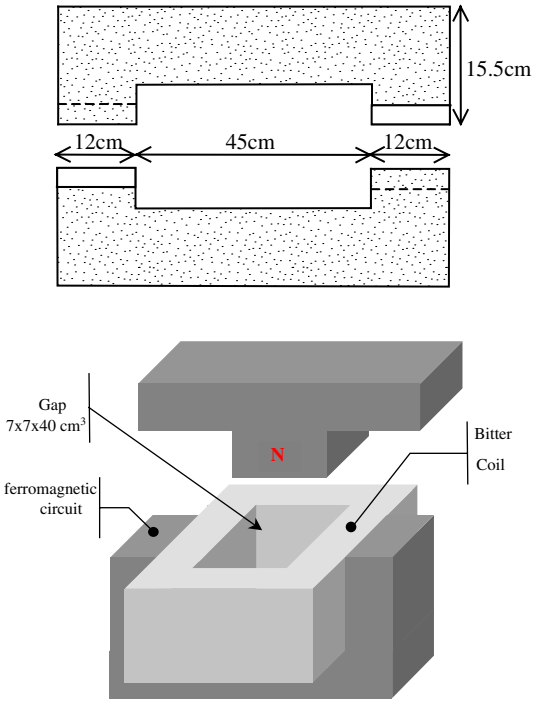

Fig. 5. Sketch of the designed electromagnet. (a) Two C-shaped copper plates before being welded together at one of their ends. (b) The Bitter coil and the ferromagnetic circuit, in open configuration.

The double-looped ferromagnetic circuit shown in Fig. 5 is made with pure iron from ARMCO™. It can be open, as represented on the figure, or closed. In this last case, the use of two loops allows the magnetic flux entering the poles to be split into two fluxes flowing in the iron on each lateral side of the solenoid. Thus even if the pole pieces are slightly saturated (e.g. with a 2 T induction) the main part of the ferromagnetic circuit is not (there, the induction is about 1T). This ferromagnetic circuit could be improved further by replacing the two pure iron pole pieces by a better magnetic material, such as a Fe–Co alloy. The design of this very compact and efficient electromagnet obviously has the disadvantage of offering poor access to the magnetised volume. The design of the furnace and the shear-cell is adapted to this constraint.

The maximum induction reached midway between the two poles is nearly 2.3 T. Fig. 6 shows induction measurements made with a Hall—gauge, for two values of the electrical current. Both measurements near and at mid-distance of the iron poles are plotted to show the homogeneity of the field. Note that the 2 mm capillary tubes of the shear cell occupies an 18 cm long region around $X = 17.5$ cm on the present plot. For a 2.15 T induction, the deviation from homogeneity in this region is about 3%, despite the saturation of the ferromagnetic circuit. The homogeneity is significantly better when lower induction is considered.

3.2. The furnace and the shear-cell: control of the temperature field in a compact device

The design of the cylindrical furnace and shear-cell unit in Euridice II is similar to that of Euridice I (see [3,5]). It is however far more compact: $\varnothing\ 65\times450$ mm^2 versus $\varnothing\ 120\times800$ mm^2 for the earlier set-up. Contrary to Euridice I, where a longitudinal temperature gradient was forced, we aim here at creating a temperature field which is as isothermal as possible at the scale of the 2×180 mm^2 capillary tubes. Here the furnace is directly screwed on the iron mass of the ferromagnetic circuit. The shear-cell itself is very similar to the one described in Part II and will not be further described in this paper. Interested readers will find more details in [5].

The interior of the furnace is a graphite thick tube. The temperature field is controlled by three individually monitored heating elements, consisting of resistive wires embedded in the graphite. One of the heating elements compensates for the side heat-losses all along the cylinder, the two smaller ones compensate for losses at the cylinder ends. A layer of super insulating material surrounds the graphite tube. Contrary to Euridice I, the exterior of the furnace is not made of stainless steel, but consists of a 5 mm thick copper tube; it is water cooled only at its two ends. Due to the excellent thermal conductivity of copper, the external temperature field and

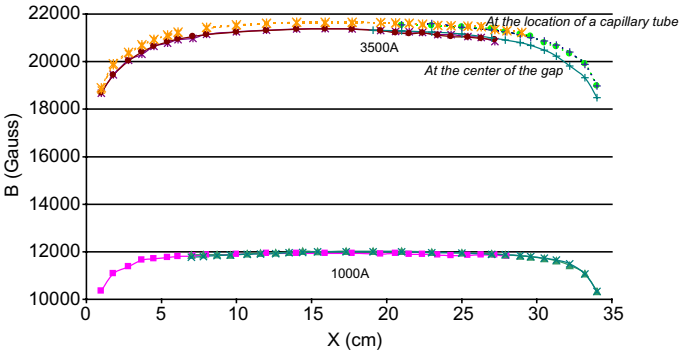

Fig. 6. Vertical component of the magnetic field measured in the gap of the electromagnet.

the radial losses can be homogenised. As described in Part II, a homogeneous temperature field is maintained by PID regulators. For a mean temperature of 275 °C, the temperature variations along the capillary are measured to be less than 0.4 °C. Axial temperature gradients deduced from these measurements are of the order of 5 °C/m. The axial temperature variations can also be used for an order-of-magnitude estimate of the radial losses. The radial temperature gradients were thus estimated to be of the order of 2 °C/m (see [14] for details).

3.3. Control of the initial composition

As fluid motion in the present experiments is mainly driven by solute buoyancy, it is important to produce homogeneous initial loads of reproducible nominal composition. A dedicated set-up has been implemented to produce $\varnothing$ 7 mm × 1 m cylinders of alloy. The solid metals are put together in a quartz crucible; as the total mass in use is about 300 g, it is possible to control accurately the weight fraction of solute (1 wt.% Bi in pure Sn in the present paper). The solvent (Sn) is taken from 5 N sources. These metals are melted by induction in an Argon gas atmosphere. Once at liquid state, the induction is also responsible for a strong stirring which, added to natural convection motions, leads to an efficient mixing of the components. A minimum of 15 min is allowed for this mixing phase. Some void is then established in the enclosure. The end of a 1 m long quartz tube is sank into the liquid (the whole set-up being of course airtight). Some Argon gas is suddenly re-introduced in the enclosure. The liquid alloy is thus pushed up into the tube which is filled within less than 1 s. A water-cooled cold-box is finally translated along the quartz tube to quench the alloy. Several samples taken from the same charge have been analysed using the inductively coupled plasma (ICP) method; a homogeneity within 4% was observed. This should be compared with the 2–3% uncertainty of the chemical analysis itself.

4. Experimental validation of the new model

Although the experimental results presented in [3] were in good agreement with the expected tendencies, they can be regarded neither as a full validation of the model nor as a good illustration of the measurement method in the most general case of a significant solutal convection. The main reason is that these earlier measurements do not show any evidence of the change in slope of the curve $D_{\mathrm{app}} = f(\alpha^{0.5}B^{-2})$ near its origin. A quantitatively good prediction of this curvature is very important for the accurate determination of diffusivities from future experiments. Validation of the theoretical model in this region is therefore the objective of the new experiments, which are performed with a stronger magnetic field, but in otherwise similar conditions. In particular, the same SnBi (1 wt.%) alloy, the same horizontal and isothermal configuration (275 °C), the same experiment durations and the same capillary diameter are used. The solutal Grashof number is thus $Gr_{\mathrm{S}} = 92$.

The chemical analysis of the samples were also performed in the same manner, and even by the same person as in the previous experiments. The least-mean-squares fit of the concentration profiles with an error function has however undergone some changes since the publication of Part II. The origin of the profile is now allowed to cross the horizontal axis at some distance x_0 from the origin. The theoretical profile is thus considered to be:

$$C_{\mathrm{th}} = \frac{1}{2} C_{\max}\left(1 + \operatorname{erf}\left(\frac{x - x_0}{2\sqrt{D_{\mathrm{app}} t}}\right)\right). \tag{20}$$

The introduction of the new parameter x_0 (the other ones being $C_{\max}$ and D_{app}) in the analysis of the data has some influence on the estimated D_{app} value. The difference between the "new" and the "old" values is observed to vary from 0% to 3%. Table 1 therefore gives the results obtained in both Euridice II and Euridice I, the latter re-analysed with the new procedure.

Table 1
Summary of the relevant experiments of diffusion of Bi (1 wt.%) in liquid Sn

Remark	$B(T)$	T (°C)	C_{max} (W%)	D_{app} (m^2/s)	x_0 (m)	χ (W%)
Euridice I	0.4	275	0.98	7.34×10^{-9}	-3.4×10^{-4}	0.065
	0.4	275	1.01	7.34×10^{-9}	-1.1×10^{-3}	0.062
	0.45	275	1.01	6.39×10^{-9}	-6.9×10^{-4}	0.060
	0.45	275	0.98	6.25×10^{-9}	-8.9×10^{-5}	0.061
	0.5	275	0.96	5.38×10^{-9}	-1.3×10^{-4}	0.048
	0.5	275	0.95	5.52×10^{-9}	3.4×10^{-5}	0.056
	0.6	275	0.99	4.54×10^{-9}	4.7×10^{-5}	0.046
	0.6	275	0.98	4.40×10^{-9}	-6.6×10^{-4}	0.049
	0.75	275	0.99	3.60×10^{-9}	-5.5×10^{-4}	0.035
	0.75	275	0.98	3.52×10^{-9}	1.1×10^{-4}	0.036
$t = 46800$ s	0.5	275	0.99	7.10×10^{-9}	9.1×10^{-5}	0.056
$t = 46800$ s	0.5	275	1.02	7.21×10^{-9}	-5.3×10^{-4}	0.063
$t = 71491$ s	0.5	275	0.98	6.25×10^{-9}	-1.8×10^{-4}	0.059
$t = 71491$ s	0.5	275	0.98	6.07×10^{-9}	-7.2×10^{-4}	0.055
Step from Euridice I to Euridice II						
$t = 46800$ s	0.5	275	0.87	7.39×10^{-9}	1.1×10^{-3}	0.052
$t = 46800$ s	0.5	275	0.86	7.12×10^{-9}	1.2×10^{-3}	0.053
	1	275	0.82	2.58×10^{-9}	1.9×10^{-3}	0.029
	1	275	0.85	2.71×10^{-9}	1.6×10^{-3}	0.032
	2	275	0.88	2.21×10^{-9}	4.1×10^{-4}	0.026
	2	275	0.87	2.15×10^{-9}	7.8×10^{-4}	0.019
	1.5	275	0.85	2.30×10^{-9}	1.3×10^{-3}	0.033
	1.5	275	0.86	2.40×10^{-9}	1.1×10^{-3}	0.031
T_{fusion} + 3–4 °C	1.5	T_f+3–4 °C	0.91	2.15×10^{-9}	2.7×10^{-4}	0.023
T_{fusion} + 3–4 °C	1.5	T_f+3–4 °C	0.91	2.17×10^{-9}	3.0×10^{-4}	0.022
T_{fusion} + 1 °C	1.5	T_f+1 °C	0.95	2.25×10^{-9}	3.0×10^{-4}	0.044

The duration of the experiments is of 26 h, unless specified. The higher part of the table relates experiments performed in the Euridice I set-up; these experiments were already presented in Part II. The lower part is dedicated to new results obtained with Euridice II. The dispersion is estimated by $\chi = \{\Sigma(C_{exp} - C_{th})^2\}^{1/2}$ where C_{th} is an error function profile (Eq. (20)).

As two different experimental set-ups are used to check one single model expression, the purpose of the first experiment in Euridice II was to check that the same experimental conditions lead to the same result. For a diffusion time of 13 h in a field of 0.5 T ($Ha = 37$), the apparent diffusion coefficients measured in Euridice I were $D_{app} = 7.1\times10^{-9}$ m^2/s and $D_{app} = 7.21\times10^{-9}$ m^2/s, while the ones measured in Euridice II were $D_{app} = 7.12\times10^{-9}$ m^2/s and $D_{app} = 7.39\times10^{-9}$ m^2/s. The largest difference is about 4%, which is comparable to the uncertainty of the D_{app} measurement. The agreement between the two experiments is thus satisfactory. These data and the results of two previous experiments in a field of 0.5 T are plotted in Fig. 7 as a function of the diffusion time. This logarithmic plot actually corresponds to Fig. 7(b) of [3]; the theoretical prediction according to Eq. (18) has been added together with the Euridice II data. Let us recall that the asymptotic analysis presented in [3] predicted a $t^{-0.5}$ time dependence. The experimental results suggested however a slightly different exponent, namely −0.4. The better agreement of the present model (Eq. (18)) is attributed to the account of longitudinal diffusion, which was neglected in the asymptotic analysis.

Fig. 8 shows a comparison between experimental results and model predictions for a fixed experiment duration of 26 h. This can be compared with Fig. 7(a) of [3]; three new data points are plotted, allowing the curve to be extended towards the origin. The magnetic field intensities used for these points were 1, 1.5 and 2 T, respectively. The drawn curve results from a two parameters least-mean-squares fit of Eq. (18) to the 16 data points. Note that two entirely different experimental apparatus were used to produce this curve. This demonstrates the repeatability of the proposed method.

The measured value of the diffusivity is $2.04 \pm 0.15 \times 10^{-9}$ m^2/s. This value is in good agreement with a recent microgravity measurement during the FOTON 12 mission [7,9]. The FOTON 12 experiment was for the simultaneous diffusion of In (0.95 wt.%) and Bi (2.5 wt.%) in liquid Sn, at a temperature of 300 °C. A comparison can be made with our results if the diffusion of In and Bi are assumed independent, and if the diffusion coefficient depends only weakly on the concentration. Since the two nominal temperatures are very close, we can account for the diffusivity temperature dependence using a kT^2 law without inducing too much error. The first raw analysis of

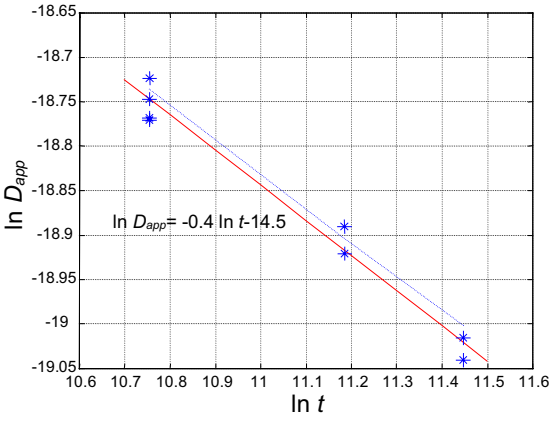

Fig. 7. Variation of the apparent diffusion coefficient with time. The experimental results (stars) have been obtained in a 0.5 T magnetic field ($Ha = 37$), the only varying parameter is the duration of the experiments. The full line is a linear interpolation of these data, its equation given in the figure. The dotted line is plotted from Eq. (18), assuming $D = 2 \times 10^{-9}$ m^2/s.

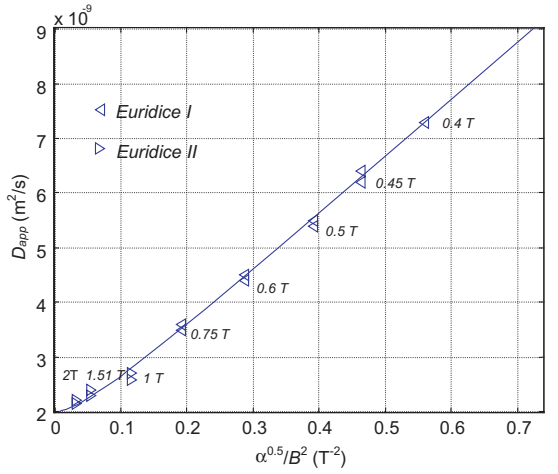

Fig. 8. Experimental results for diffusion of Bi (1 wt.%) in Sn. The diffusion time is 26 h. The magnetic induction used in each experiment is tagged near the corresponding points. The experimental points are issued from two different apparatus. The full line is the prediction of the present model (Eq. (18) after a least-mean-squares fit to the experimental data).

the FOTON 12 mission, presented in [7], gives the diffusion coefficient $2.3 \pm 0.3 \times 10^{-9}$ m^2/s at 300 °C. This then corresponds to 2.1×10^{-9} m^2/s at 275 °C, for comparison with our results. Note that a more detailed analysis of the FOTON 12 experiment is to be published in the near future [8], although these results are not expected to change significantly. The diffusion coefficient for diffusion of In in Sn measured during the same space experiment is also in good agreement with the values reported in [3].

A comparison with the directional solidification experiments in the Mephisto apparatus [9,10] provides a less coherent picture. The two considered space experiments performed on a Sn Bi(0.58 at.%) alloy provided diffusivity values of 1.3×10^{-9} m^2/s [9] and 1.5×10^{-9} m^2/s [10] at the fusion temperature. These values are smaller than both the FOTON 12 and the Euridice values, after extrapolation to the fusion temperature by a kT^2 law. The same quenched solidification technique had already been used by Verhoeven et al. [11] in ground-based experiments. The latter results are compatible with the FOTON 12 and Euridice values. Some effort has been made to investigate the sensitivity of directional solidification diffusivity measurement to other parameters [5] (such as the partition coefficient, the nominal concentration, or the solidification rate). It has been observed in particular that a change in bulk concentration from 0.58 to 0.56 at.% may lead to a 10% change on the measured diffusivity. The quenched solidification technique is not dedicated method for the measurement of diffusivities; the results depend on numerous parameters and, in our opinion, should be considered with some caution.

The comparison with the quenched solidification measurements relies on the assumption that the diffusion coefficient follows a kT^2 law. The question then arises whether such a law is valid, especially near the fusion point. Two more experiments were therefore performed at a temperature measured to be less than 5 °C above the fusion point. The duration of these experiments was still 26 h and the magnetic field was 1.5 T. Three apparent diffusion coefficients were obtained from these experiments, although four capillaries were processed. The fourth tube suffered from a bad filling, leading to the presence of bubbles and free surfaces, and it was not analysed. The three measured diffusion coefficients are respectively: $D_{\text{app}} = 2.15 \times 10^{-9}$, 2.17×10^{-9} and 2.25×10^{-9} m^2/s. For this value of the magnetic field, it can be estimated from Fig. 8 that the apparent diffusion coefficient is about 20% higher than the true value. Assuming the same distance for the present three experiment leads to an estimate of the diffusivity at the fusion point of 1.7×10^{-9} m^2/s. This value is consistent with our other experimental results plotted in Fig. 8 if a kT^2 behaviour is assumed. No significant departure from a kT^2 law is thus observed.

5. Conclusion

The objective of this work is to account for the practically unavoidable presence of convection in liquid metals diffusion experiments. The method relies on an accurate modelling of the convective transport, rather than its complete suppression. Controlling the convective flow is essential to the success of the method; a magnetic field is an effective tool for achieving such

control in highly conducting liquids, such as metals and semiconductors.

Earlier efforts presented in [2,3] mainly focus on the asymptotic cases of negligible or fully dominant solutal convection, i.e. for S^2/τ much smaller or much greater than 1, respectively. The present paper proposes a single analytical model covering the whole range of S^2/τ from solutal convection dominated transport to quasi-diffusive transport. This model predicts the apparent diffusion coefficient measured in a particular experiment. The model, which appears to be in good agreement with the numerical solution of the 1D transport equation, relies on two assumptions:

- The duration of the experiment is much larger than the solute diffusion time at the scale of the cross-section:

  $t \gg H^2/D.$

- The concentration profile can be compared with a known self-similar function. A good choice is shown to be:

  $c = c_{\max}/2\mathrm{erf}[x/(4D_{\mathrm{app}}t)^{1/2}].$

The model is tested against experimental results concerning impurity diffusion of Bi in Sn. The model is in good agreement with data obtained in two different experimental apparatus. The dispersion is only a few percent, and the measured values are in good agreement with recent space experiments.

The presented experimental results demonstrate that accurate ground-based measurements can be obtained by convection control. The accuracy of the new method is estimated to be at least similar to other classical methods (see [5,8] for more details). Moreover, the relatively low cost of the method allows a statistical treatment of a larger number of experiments. An important feature of the method is that the measured diffusion coefficient can be plotted versus some quantification (here $\alpha^{1/2}/B^2$) of the level of convection. As a consequence, any significant uncontrolled convection should be detected as a departure from the analytical prediction (Ref. [14] provides an actual example of such a diagnostic). This is not possible in experiments relying on the achievement of purely diffusive conditions, since there is no diagnostic tool for verifying the actual absence of convection.

The two tin alloys used in the present work can be seen to represent liquid metals that are relatively easy to handle. Some challenges with other materials are the following:

(a) The solutal convection may be stronger than for SnBi (1 wt.%), which has a solutal expansion coefficient of 0.3 wt.%$^{-1}$. Some metallic alloys have solutal expansion coefficients as high as 2 wt.%$^{-1}$. As a consequence, the Grashof numbers to be reached may be 10 times larger than in the present experiments. This corresponds to factor 3 increase of the desired magnetic field intensity; a magnetic field of 6 T requires superconducting magnets.

(b) A number of future experiments should be operated at higher temperatures than ours (<300 °C). From a technical standpoint, the control of the thermal field in the set-up is all the more difficult as the temperature level is high. Compromises will thus have to be made regarding minimisation of the magnetised volume and the bulk of the furnace. One must keep in mind that the Ha^{-2} natural convection braking law is submitted to the symmetry of the different fields entering the problem and of the geometry with respect to a horizontal plan [12,14].

(c) Finally, difficulties may arise related to chemical reactions between the liquid and the crucible. These problems are of course not unique to the present method, but here the choice of the crucible materials is limited to non-conducting media.

The present approach could be generalised to deal also with non-conducting materials. The principle of the model would be the same, but the control of the convection would have to be achieved by some non-electromagnetic force-field; the use of rotation as an analogue for the magnetic field is for example proposed by Alboussière [13].

Acknowledgements

This program has been achieved with the support of the CNES (Centre National d'Etudes Spatiales) and the CNRS (Centre National de la Recherche Scientifique). Special thanks to J.P. Garandet, T. Alboussière and D.J. Maclean for daily and fruitful collaboration on the subject. The authors would also like to thank the Chemical Analysis Center of the CNRS, and especially Mr Imbert and Mr Duteil, for the quality of their ICP analysis. The members of the ESA topical team *Transport Properties in liquids* are deeply acknowledged for the discussions on diffusion measurements. O. Cugat and J. Delamare provided good advice for the design of the electromagnet. Finally, warm thanks to Esther for the part she took in typing these lines, and to Ola Widlund for helping in the revision of the manuscript.

References

[1] T. Iida, R.I.L. Guthrie, The physical properties of liquid metals, Oxford Science Publishers, 1988.

[2] D.J. Maclean, T. Alboussière, Measurement of solute diffusivities. Part I: Analysis of coupled solute buoyancy-

driven convection and mass transport, Int. J. Heat Mass Transfer 44 (17) (2001) 1639–1648.

[3] V. Botton, P. Lehmann, R. Bolcato, R. Moreau, R. Haettel, Measurement of solute diffusivities. Part II: Experimental measurements in a convection controlled shear cell. Interest of a uniform magnetic field, Int. J. Heat Mass Transfer 44 (2001) 3345–3357.

[4] C. Barat, J.-P. Garandet, The effect of natural convection in liquid phase mass transport coefficient measurements: the case of thermosolutal convection, Int. J. Heat Mass Transfer 39 (10) (1996) 2177–2186.

[5] V. Botton, Une méthode pour mesurer, au sol, la diffusion d'impureté dans les métaux liquides, Ph.D. thesis, INP Grenoble, 2001.

[6] J.-P. Praizey, Benefits of microgravity for measuring thermotransport coefficients in liquid metallic alloys, Int. J. Heat Mass Transfer 32 (12) (1989) 2385–2401.

[7] J.-P. Garandet, P. Dusserre, J.-P. Praizey, J. Abadie, A. Griesche, V. Botton, Measurement of solute diffusivities in liquid metal alloys within the AGAT facility during the FOTON 12 mission, J. Microgravity Space Station Utilisation 1 (2000) 29–34.

[8] J.P. Garandet, G. Mathiak, V. Botton, P. Lehmann, A. Griesche, Reference microgravity measurements of solute diffusivities in tin and aluminium based alloys, Int. J. Thermophys., in press.

[9] J.-J. Favier, P. Lehmann, J.-P. Garandet, B. Drevet, F. Herbillon, On the measurements of thermophysical properties during planar front solidification of an SnBi alloy in microgravity: results of the MEPHISTO-USMP1 Experiments, Acta. Mater. 44 (12) (1996) 4899–4907.

[10] G. Boutet, Utilisation du diagnostic Seebeck pour le suivi des phénomènes interfaciaux en solidification et fusion dirigée: application à une expérience spatiale, Ph.D. thesis, Université Paris VI, 1999.

[11] J.D. Verhoven, E.D. Gibson, R.I. Griffith, Measurement of liquid metal diffusion coefficients from steady-state solidification experiments, Metall. Trans. B 6B (1975) 475–479.

[12] T. Alboussière, J.-P. Garandet, R. Moreau, Asymptotic analysis and symmetry in MHD convection, Phys. Fluids 8 (8) (1996) 2215–2226.

[13] T. Alboussière, Rotating shear cell, Personal communication, 27th September 1999.

[14] V. Botton, P. Lehmann, The striking effect of residual temperature gradients on liquid metals solute diffusion coefficients measurement, Int. J. Thermophys., submitted for publication.